

# UCLA

## UCLA Previously Published Works

### Title

Therapeutic IDOL Reduction Ameliorates Amyloidosis and Improves Cognitive Function in APP/PS1 Mice

### Permalink

<https://escholarship.org/uc/item/8ds76367>

### Journal

Molecular and Cellular Biology, 40(8)

### ISSN

0270-7306

### Authors

Gao, Jie  
Littman, Russell  
Diamante, Graciela  
et al.

### Publication Date

2020-03-30

### DOI

10.1128/mcb.00518-19

Peer reviewed



# Therapeutic IDOL Reduction Ameliorates Amyloidosis and Improves Cognitive Function in APP/PS1 Mice

Jie Gao,<sup>a</sup> Russell Littman,<sup>b,c</sup> Graciela Diamante,<sup>b</sup> Xu Xiao,<sup>f</sup> In Sook Ahn,<sup>b</sup> Xia Yang,<sup>b,c,d</sup> Tracy A. Cole,<sup>e</sup> Peter Tontonoz<sup>f</sup>

<sup>a</sup>Department of Neuroscience, The Ohio State University Wexner Medical Center, Columbus, Ohio, USA

<sup>b</sup>Department of Integrative Biology and Physiology, University of California—Los Angeles, Los Angeles, California, USA

<sup>c</sup>Bioinformatics Interdepartmental Program, University of California—Los Angeles, Los Angeles, California, USA

<sup>d</sup>Institute for Computational and Quantitative Biosciences, University of California—Los Angeles, Los Angeles, California, USA

<sup>e</sup>Central Nervous System Group, Antisense Drug Discovery, Ionis Pharmaceuticals, Inc., Carlsbad, California, USA

<sup>f</sup>Department of Pathology and Laboratory Medicine, David Geffen School of Medicine, University of California—Los Angeles, Los Angeles, California, USA

**ABSTRACT** Brain lipoprotein receptors have been shown to regulate the metabolism of ApoE and  $\beta$ -amyloid ( $A\beta$ ) and are potential therapeutic targets for Alzheimer's disease (AD). Previously, we identified E3 ubiquitin ligase IDOL as a negative regulator of brain lipoprotein receptors. Genetic ablation of *Idol* increases low-density lipoprotein receptor protein levels, which facilitates  $A\beta$  uptake and clearance by microglia. In this study, we utilized an antisense oligonucleotide (ASO) to reduce IDOL expression therapeutically in the brains of APP/PS1 male mice. ASO treatment led to decreased  $A\beta$  pathology and improved spatial learning and memory. Single-cell transcriptomic analysis of hippocampus revealed that IDOL inhibition upregulated lysosomal/phagocytic genes in microglia. Furthermore, clustering of microglia revealed that IDOL-ASO treatment shifted the composition of the microglia population by increasing the prevalence of disease-associated microglia. Our results suggest that reducing IDOL expression in the adult brain promotes the phagocytic clearance of  $A\beta$  and ameliorates  $A\beta$ -dependent pathology. Pharmacological inhibition of IDOL activity in the brain may represent a therapeutic strategy for the treatment of AD.

**KEYWORDS** Alzheimers, IDOL, LXR, macrophage, microglia

The *APOE* genotype is the strongest genetic risk factor for Alzheimer's disease (AD). ApoE has been shown to independently influence several key factors that drive pathogenesis of AD, including  $\beta$ -amyloidosis, tauopathy, and synaptic dysfunction (1–3). The impact of ApoE on amyloidosis has been the subject of intensive research, since  $\beta$ -amyloid ( $A\beta$ ) accumulation and aggregation are key initiators of complex pathological changes in the brain that culminate in neurodegeneration years later. Mounting evidence suggests that ApoE primarily influences AD pathology via its effects on  $A\beta$  metabolism. ApoE exerts the greatest impact on amyloidosis during the initial seeding stage; accordingly, lowering ApoE levels prior to the formation of  $A\beta$  plaque in APP/PS1 mice reduces  $A\beta$  plaque pathology (4). ApoE has also been reported to promote  $A\beta$  aggregation (5) and to impair its clearance from the brain interstitial fluid (6).

In the brain, ApoE functions as a ligand for members of the lipoprotein receptor family, including low-density lipoprotein receptor (LDLR), LDL receptor-related protein 1 (LRP1), very low-density lipoprotein receptor (VLDLR), and ApoE receptor 2 (ApoER2). Among ApoE receptors, LDLR and neuronal LRP1 are the principal regulators of ApoE metabolism, acting to mediate the uptake and degradation of ApoE-containing lipoprotein particles by brain cells (7). Overexpression of the LDLR in glia cells reduces brain

**Citation** Gao J, Littman R, Diamante G, Xiao X, Ahn IS, Yang X, Cole TA, Tontonoz P. 2020. Therapeutic IDOL reduction ameliorates amyloidosis and improves cognitive function in APP/PS1 mice. *Mol Cell Biol* 40:e00518-19. <https://doi.org/10.1128/MCB.00518-19>.

**Copyright** © 2020 American Society for Microbiology. All Rights Reserved.

Address correspondence to Jie Gao, Jie.Gao@osumc.edu, or Peter Tontonoz, PTontonoz@mednet.ucla.edu.

**Received** 21 October 2019

**Returned for modification** 9 November 2019

**Accepted** 11 January 2020

**Accepted manuscript posted online** 21 January 2020

**Published** 30 March 2020

ApoE and A $\beta$  deposition level by enhancing A $\beta$  clearance (8), suggesting that increasing glial LDLR levels may represent a therapeutic strategy to treat AD.

We previously identified E3 ubiquitin ligase IDOL as a negative regulator of LDLR in microglia. Loss of IDOL in microglia increases LDLR protein levels, which in turn facilitates ApoE and A $\beta$  uptake and clearance by microglia. Ablation of IDOL in both male and female APP/PS1 mice—a transgenic mouse model of A $\beta$  amyloidosis—led to decreased soluble and insoluble A $\beta$ , reduced amyloid plaque burden, and ameliorated neuroinflammation (9). Whether pharmacological inhibition of IDOL in the adult brain can serve as a safe and effective therapeutic strategy to ameliorate A $\beta$ -related pathology remains to be determined. In this study, we utilized an antisense oligonucleotide (ASO) to therapeutically inhibit IDOL activity in the adult brain of APP/PS1 mouse model of AD amyloidosis. IDOL ASO treatment reduced soluble and insoluble A $\beta$  and amyloid plaque load in the brain and also decreased neuritic dystrophy around plaques. Importantly, IDOL ASO treatment also improved the cognitive performance of APP/PS1 mice in the Morris water maze. Our results provide validation of the potential utility of IDOL as a therapeutic target for AD pathogenesis.

## RESULTS

**ASO treatment reduces IDOL expression *in vivo*.** We optimized a central nervous system (CNS)-acting ASO against IDOL to enable the inhibition of IDOL activity in the adult mouse brain. To evaluate the efficacy of the anti-IDOL ASO (here referred to as IDOL ASO) and determine the optimal dose, five groups of C57BL/6J male mice ( $n = 5$  for each group) received intracerebroventricular (i.c.v.) injection of various doses of IDOL ASO or PBS (vehicle control) into the lateral ventricle. After a 2-week incubation, we measured IDOL mRNA level in total brain lysates. IDOL ASO showed high potency with half-maximal inhibitory concentration ( $IC_{50}$ ) of 12.5  $\mu$ g/mice and prolonged stability with an estimated half-life ( $t_{1/2}$ ) of 9 weeks (Fig. 1A). A single bolus dose of 40  $\mu$ g of IDOL ASO reduced IDOL mRNA level by at least 80% relative to controls by qPCR, and knockdown of IDOL was seen in all the brain regions examined, including the hippocampus, cortex, thalamus, and cerebellum (Fig. 1B). We chose a 40  $\mu$ g of IDOL ASO i.c.v. injection every 2 to 3 months as the optimal treatment strategy for the following studies. This approach achieves close to maximum IDOL knockdown efficiency with minimal amount of ASO, thereby minimizing nonspecific effects. Since IDOL is mainly expressed in the microglia and neurons, we examined the cellular uptake of ASO by immunohistochemical staining of brain sections with a pan-ASO antibody (Fig. 1C). This analysis showed that the ASO was taken up by both microglia and neurons. Consistent with reduced IDOL expression, the protein level of IDOL substrates—LDLR, VLDLR, and ApoER2—were all increased in the brains of IDOL ASO-treated mice (Fig. 1D), despite the fact that their mRNA levels remain unchanged (data not shown). We did not observe changes in body weight or gross behavior associated with IDOL ASO treatment in our study. When evaluated in contextual fear conditioning and the Morris water maze, IDOL ASO treatment did not affect the cognitive performance of wild-type mice (Fig. 1E and F).

**IDOL-ASO treatment ameliorates A $\beta$  plaque pathology.** To assess the effects of brain IDOL inhibition on amyloidosis in an AD mouse model, we administered IDOL ASO (40  $\mu$ g/mouse) or vehicle (phosphate-buffered saline [PBS]) via i.c.v. injection to a cohort of APP/PS1 male mice ( $n = 8$  to 10 per group) at 3 months of age (before the onset of plaque formation), followed by a booster dose at 6 months of age. Mice were sacrificed at 8 to 9 months of age and brains were collected for pathological analysis. We first assessed A $\beta$  deposition by immunostaining with an anti-A $\beta$  antibody (82E1). A $\beta$  plaque area in IDOL ASO-treated APP/PS1 mice was reduced >50% compared to controls (Fig. 2A). Quantification of fibrillar plaque load using X-34 dye also showed a marked reduction (>50%) in the ASO-treated group (Fig. 2B). Next, we biochemically assessed A $\beta$ 40 and A $\beta$ 42 levels in radioimmunoprecipitation assay (RIPA; soluble) and Guan (insoluble) fractions of brain lysates. IDOL ASO treatment reduced A $\beta$ 40 and A $\beta$ 42 load in both soluble and insoluble fractions in APP/PS1 mice (Fig. 2C and D). Western

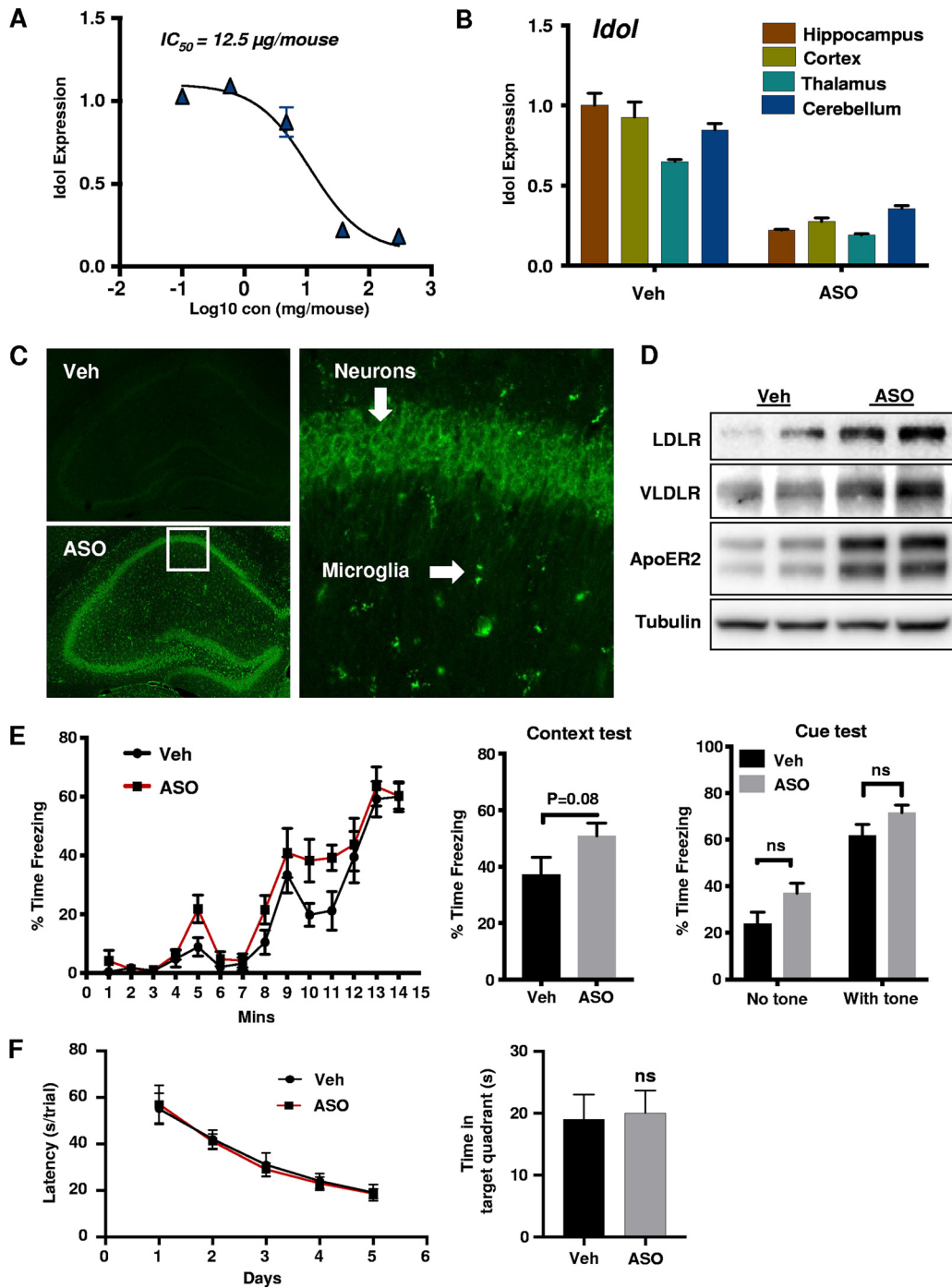


**FIG 1** (A) IDOL ASO administration via i.c.v. bolus injection led to dose-dependent reduction of IDOL mRNA levels in the brains of C56BL/6j mice. (B) IDOL ASO (40  $\mu\text{g}$ ) administration suppresses the IDOL mRNA level across different brain regions detected by RT-PCR. (C) Immunofluorescent staining of brain sections from PBS- or ASO-treated APP/PS1 mice. Primary antibody against the general backbone of ASOs (a gift from Ionis Pharmaceuticals) was used to visualize the distribution of ASOs in brain cells. ASOs (green) are taken up by both neurons and microglia (arrows). (D) Representative Western blot analysis of total protein lysate from brains of WT mice. (E) Average freezing behavior during the fear conditioning training (left), average freezing behavior over 5 min, 24 h after training, in the same context in which training was carried out on day 1 (middle), and average freezing behavior in the different context 48 h after training (right). The tone was played for the last 2 min. All values are expressed in means  $\pm$  the standard errors of the mean (SEM), using two-way repeated-measures ANOVA for statistical analysis (\*,  $P < 0.05$ ; \*\*,  $P < 0.01$ ). (F) Escape latency to find the hidden platform during training trials of wild-type mice in the Morris water maze ( $n = 5/\text{group}$ ) (left) and time spent in the target quadrant searching for the hidden platform within a 1-min test duration ( $n = 5/\text{group}$ ) (right).

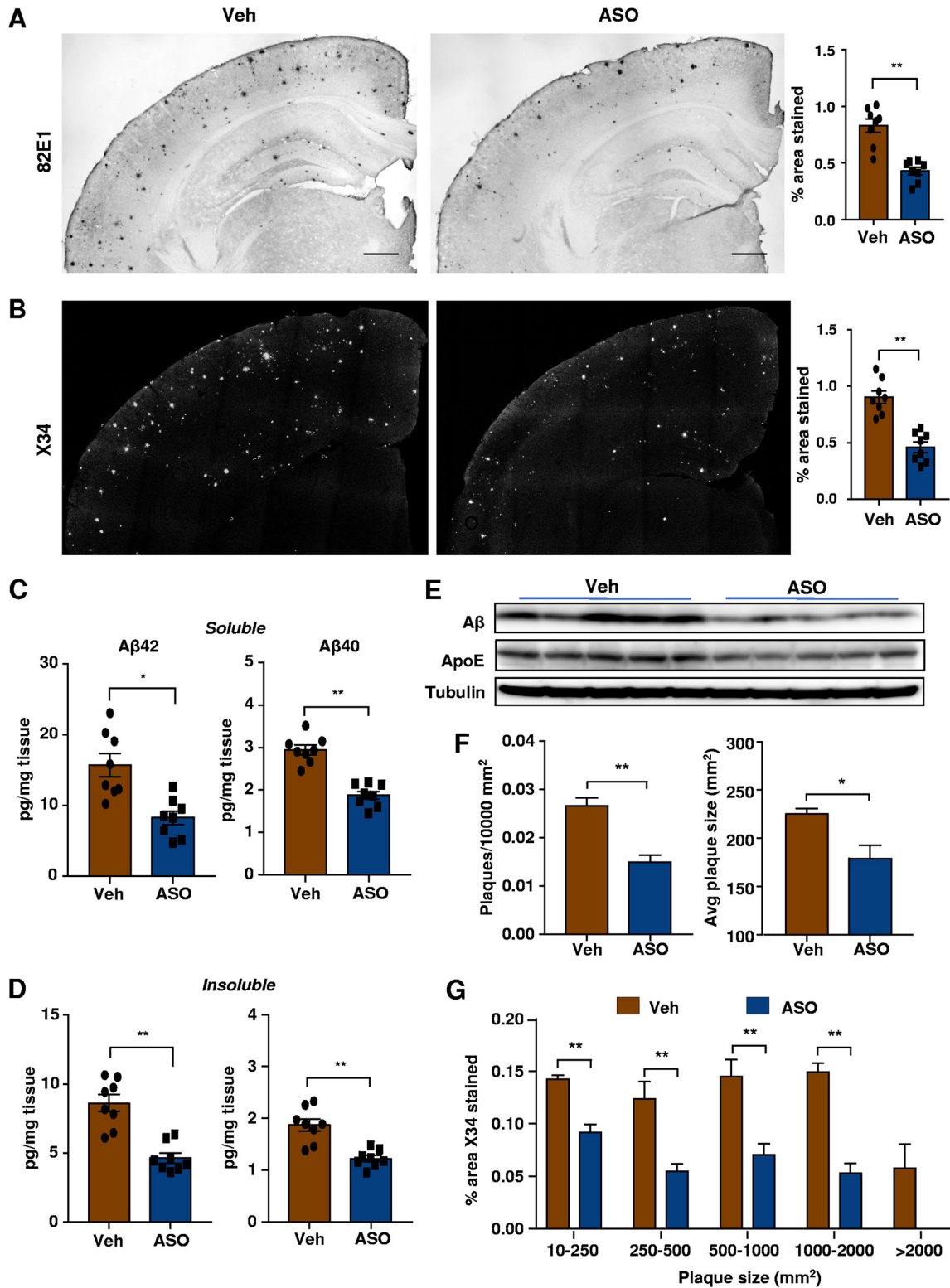


**FIG 2** (A) Brain sections from APP/PS1 mice were immunostained with anti-A $\beta$  antibody 82E1, and the extent of A $\beta$  deposition was quantified from the cortex (right). (B) Brain sections from the same cohort were stained with X-34 dye, and the fibrillar plaque load was quantified (right). \*,  $P < 0.05$ ; \*\*,  $P < 0.01$ . (C) Soluble (RIPA fraction) A $\beta$ 40 and A $\beta$ 42 levels were measured from the cortex. (D) Insoluble (guanidine fraction) A $\beta$ 40 and A $\beta$ 42 levels were measured from the same cohort ( $n = 8$  per group). \*,  $P < 0.05$ ; \*\*,  $P < 0.01$ . (E) Western blot analysis of A $\beta$  and ApoE from RIPA fractions of cortical lysates. (F) The densities of A $\beta$  antibody-stained plaques and average plaque sizes were analyzed in the same cohort of mice. (G) Analysis of plaque distribution based on size and the total area covered by plaques in each group. \*,  $P < 0.05$ ; \*\*,  $P < 0.01$ .

blot analysis of RIPA fractions of brain lysates further confirmed that IDOL ASO treatment led to reduction of total amyloid species and ApoE levels (Fig. 2E).

To examine the effects of IDOL knockdown on plaque size distribution, we analyzed the X34-stained data set by grouping individual plaques based on size. We found reduced plaque density and average size in the IDOL ASO group compared to controls (Fig. 2F). We also observed a shift in the size distribution of the plaques between groups. The total area covered by larger plaques ( $>1,000 \mu\text{m}^2$ ) was dramatically reduced, and plaques larger than  $2,000 \mu\text{m}^2$  were only rarely observed in the ASO group (Fig. 2G). Together, these results suggested that pharmacological inhibition of brain IDOL activity is sufficient to reduce  $A\beta$  levels and plaque burdens in APP/PS1 mice. These consequences of acute IDOL knockdown are consistent with our previous findings of reduced AD-like pathology in IDOL-deficient APP/PS1 mice (9).

Plaque-associated neuritic dystrophy—a well-described consequence of  $A\beta$ -induced neurotoxicity—is a key feature of pathological processes downstream  $A\beta$  in AD (10). To investigate the effects of brain IDOL inhibition on plaque-associated neurotoxicity *in vivo*, brain sections of control or IDOL ASO-treated APP/PS1 mice were costained with X-34 and an antibody against lysosomal-associated membrane protein 1 (LAMP1), a marker of dystrophic neurites. IDOL ASO-treated mice showed a reduction in the volume of dystrophic neurites (Fig. 3A). We also costained brain sections with X-34 and amyloid precursor protein (APP; another marker of dystrophic neurites) (11) and again found a reduction in the volume of plaque-associated dystrophic neurites in IDOL ASO-treated mice (Fig. 3B). These results suggest that IDOL inhibition in brain ameliorates plaque-associated neuritic dystrophy.

Glial cells, including microglia and astrocytes, play essential roles in neuroinflammation and are believed to be responsible for neuronal toxicity and synaptic dysfunction downstream of  $A\beta$ . To determine the extent of  $A\beta$ -mediated gliosis in control and IDOL ASO-treated mice, we examined anti-glial fibrillary acidic protein (anti-GFAP)-positive reactive astrocytes in mice by immunostaining. The IDOL ASO group had fewer GFAP-positive astrocytes than controls (Fig. 4A), consistent with the effects of IDOL ASO on amyloid plaque load. To evaluate the changes in the microglial response to amyloid plaque, we performed histological staining for ionized calcium-binding receptor 1 (Iba1), a marker of activated microglia. Plaque-associated microglial activation was evident around  $A\beta$  deposits in both groups. However, when corrected with plaque area, analysis of the Iba1-positive area did not reveal differences between treatment and control groups (Fig. 4B). Microglia localized in close proximity to  $A\beta$  plaques were distributed in a circumferential pattern around the plaque periphery and showed an enlarged cell body size (Fig. 4C), a feature typical of amoeboid microglia with enhanced phagocytic capacity. Interestingly, microglia in the IDOL ASO-treated group were less hypertrophic and displayed a reduced cell body size compared to those in the vehicle-treated group (Fig. 4C).

**IDOL ASO treatment improves cognitive function in APP/PS1 mice.** To determine whether reduced plaque load in ASO-treated APP/PS1 mice affected cognitive functions, including the ability to learn, we treated another cohort of APP/PS1 male mice ( $n = 12$  per group) with IDOL ASO. Two groups of mice were administered IDOL ASO ( $40 \mu\text{g}/\text{mice}$ ) or vehicle (PBS) at 3 months of age (before the onset of plaque formation), followed by two booster doses at 6 and 9 months of age. Mice were then subjected to behavioral testing at 10 months of age. We first examined hippocampus-dependent spatial memory acquisition with the Morris water maze (12). APP/PS1 mice were trained to memorize the location of a hidden, submerged platform in a water-filled pool over a 5-day period. The ASO-treated group required less time to reach the platform compared to the control group on days 4 and 5 (Fig. 5A). To determine the degree of reliance of the mice on spatial versus nonspatial cues to find the platform, we performed probe trials on day 6 in which the platform was removed. The ASO-treated group spent more time and traveled longer distances (Fig. 5B) in the quadrant of the submerged platform. These results suggested that IDOL-ASO treatment improves

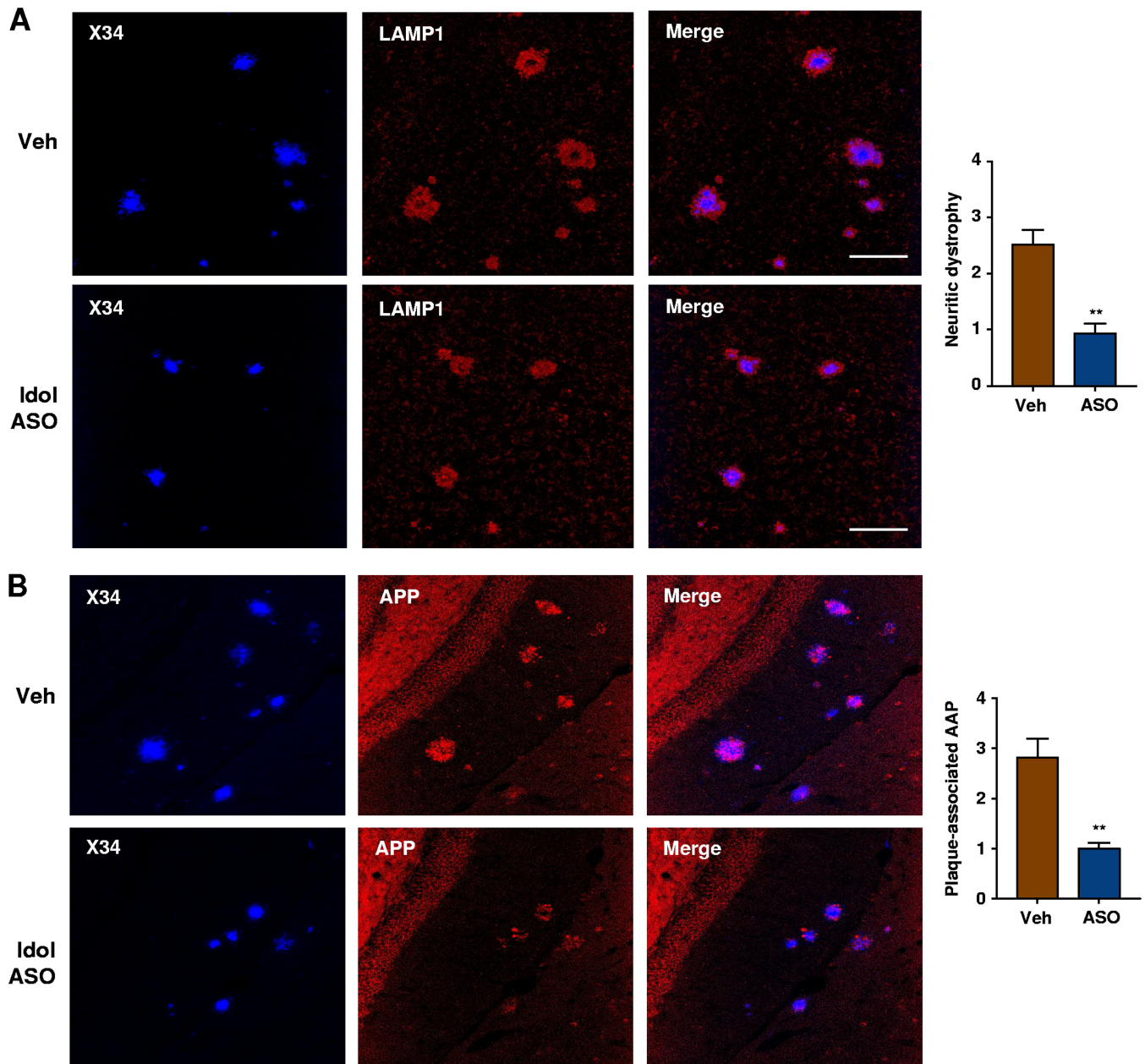


**FIG 3** (A) Representative images of brain sections from PBS- or IDOL ASO-treated APP/PS1 mice stained with LAMP1 (scale bars, 100  $\mu$ m), and the volume of LAMP1 staining in cortex was quantified ( $n = 8$  per group). (B) Representative images of brain sections from PBS- or IDOL ASO-treated APP/PS1 mice costained with X-34 and APP, and the volume of APP staining associated with amyloid plaques was quantified ( $n = 8$  per group).

spatial memory acquisition in APP/PS1 mice. This improvement in performance could not be attributed to vision or locomotor differences, since both groups performed similarly in the visible platform test (Fig. 5C, left) and exhibited comparable swimming speed (Fig. 5C, right).

We next tested cued and contextual-fear conditioning, a paradigm that assesses hippocampus-dependent (context) and amygdala-dependent (context and cued) fear learning (13) in vehicle- and IDOL ASO-treated APP/PS1 mice. On day 1, mice were trained to associate environment and sound with a foot shock. On day 2, mice were placed back into the same environment and assessed for freezing for 5 min to evaluate the contextual association with the foot shock. On day 3, mice were placed in a novel environment for 6 min and assessed for freezing during the last 3 min, when the same

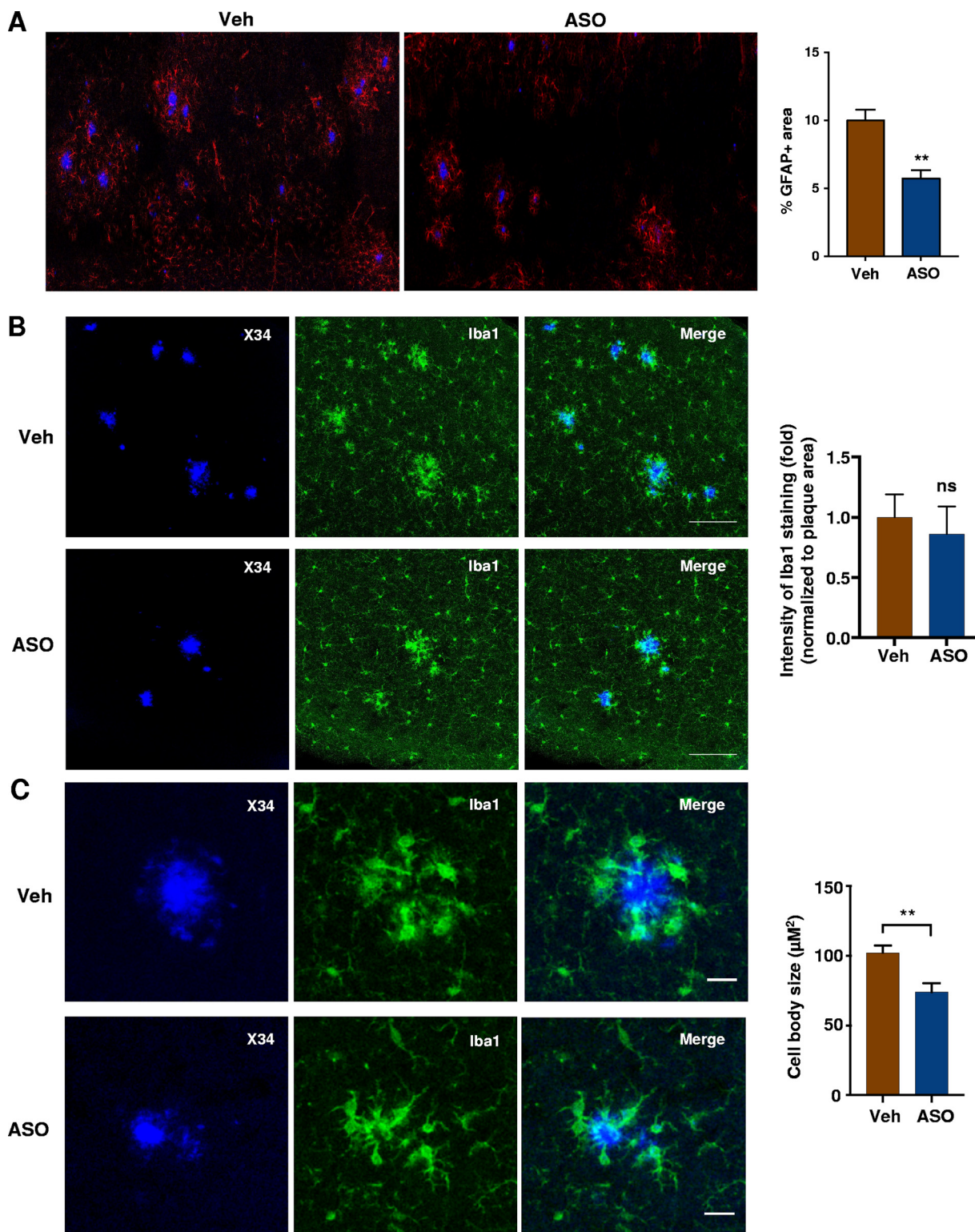


**FIG 4** (A) Representative images of brain sections from PBS- or IDOL ASO-treated APP/PS1 mice costained with X-34 and GFAP, and the volume of GFAP staining was quantified ( $n = 8$  per group). \*,  $P < 0.05$ ; \*\*,  $P < 0.01$ . (B) Representative images of brain sections from PBS- or IDOL ASO-treated APP/PS1 mice stained with Iba1 (scale bars,  $100 \mu\text{m}$ ), and the volume of Iba1 staining normalized to the plaque size was quantified ( $n = 8$  per group). (C) Representative images of brain sections from PBS- or IDOL ASO-treated APP/PS1 mice stained with Iba1 (scale bars,  $10 \mu\text{m}$ ), and the diameters of the microglia cell bodies around the plaques were quantified ( $n > 50$  microglia from each mouse, and eight mice for each group were measured). \*,  $P < 0.05$ ; \*\*,  $P < 0.01$ .

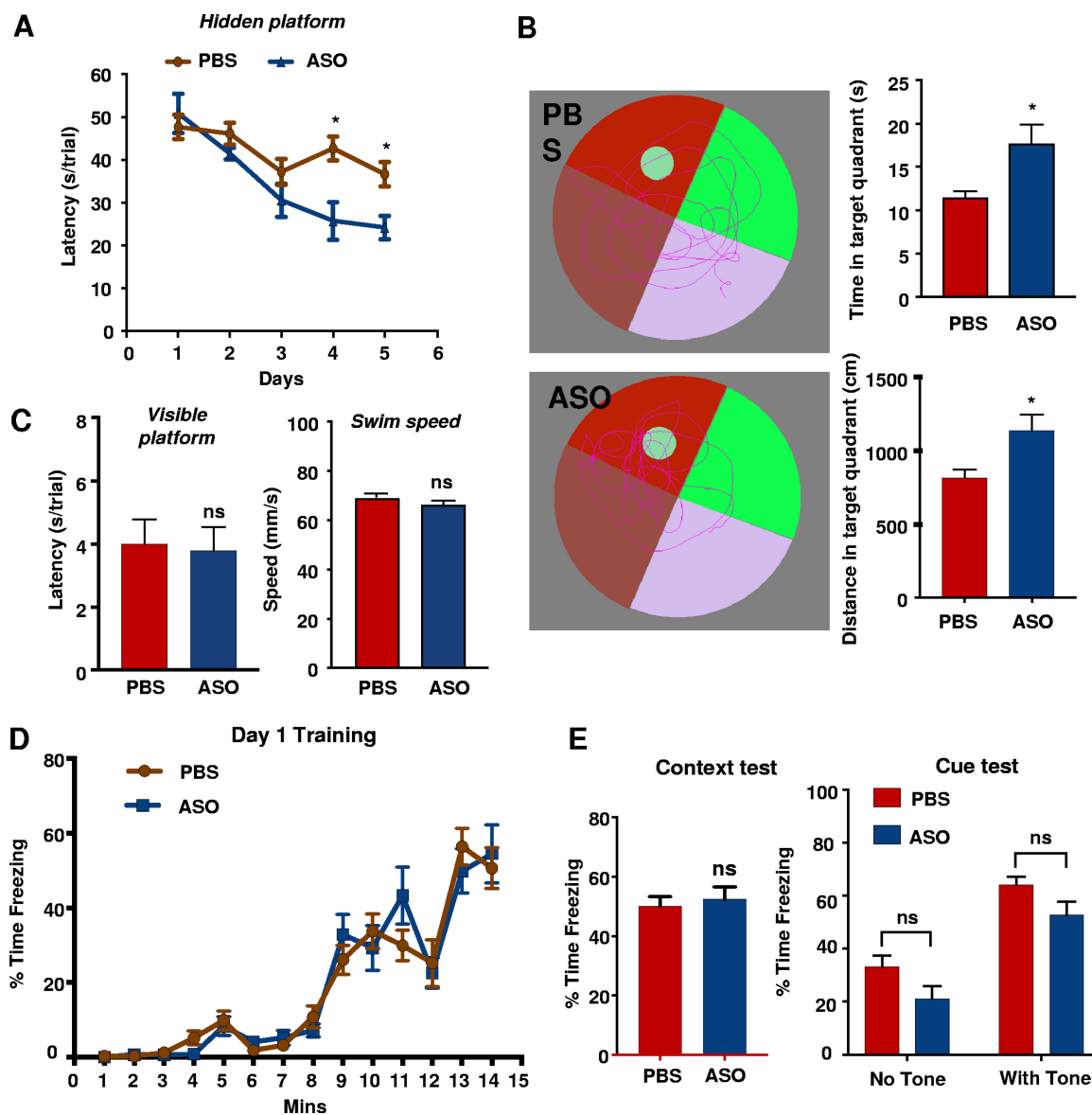


**FIG 5** (A) Escape latency to find the hidden platform during training trials of APP/PS1 mice in the Morris water maze ( $n = 12/\text{group}$ ). (B) Representative swimming path of APP/PS1 mice treated with PBS or IDOL ASO (left) and time or distance spent in the target quadrant searching for the hidden platform within 1 min test duration ( $n = 12/\text{group}$ ) (right). \*,  $P < 0.05$  (one-way ANOVA with repeated measures). (C) Escape latency to find the visible platform and swimming speeds of APP/PS1 mice in each group. (D) Average freezing behavior during the fear conditioning training. (E) Average freezing behavior over 5 min, 24 h after training, in the same context in which training was carried out on day 1 (left), and average freezing behavior in the different context 48 h after training. A tone was played for the last 2 min (right). All values are expressed as means  $\pm$  the SEM, using two-way repeated-measures ANOVA for statistical analysis. \*,  $P < 0.05$ ; \*\*,  $P < 0.01$ .

tone was played to measure the association of tone with foot shock. Both groups of mice displayed similar freezing behavior during training (Fig. 5D). On days 2 and 3, both groups showed a high level of freezing when returned to the same context or presented with the same tone. ASO-treated mice were not different from control mice in their ability to memorize the association between shock and the context (Fig. 5E, left) or auditory cue (Fig. 5E, right). The failure to detect a difference in this test may be due to the fact that performance in both groups was comparable to wild-type mice (Fig. 1E).

**Single cell RNA sequencing reveals enhanced phagocytic function of microglia in IDOL knockdown mice.** Local environmental cues are critical for shaping and maintaining brain microglial phenotypes in both mice and humans (14, 15). Furthermore, recent studies have highlighted the heterogeneity of microglial populations

during brain development (16), in different brain regions (17), and in various disease states (18). We previously showed that loss of IDOL facilitates A $\beta$  uptake and clearance by microglia *in vitro* (9). However, the role of IDOL in the function of microglia within physiological environments has not been investigated. To better capture heterogeneity of microglia and other brain cells, we used single-cell RNA sequencing (scRNA-seq) to profile the transcriptome of individual cells in mouse hippocampus. Hippocampal cells from PBS- and ASO-treated APP/PS1 mice ( $n = 3/\text{group}$ ) were isolated 1 week after behavior testing, and subjected to scRNA-seq with the Drop-seq platform (19). We obtained data for a total of 14,682 cells (6,888 from the PBS group and 7,794 from the ASO-treated group) after quality control filtering.

We clustered the hippocampal cells based on their similarities in gene expression pattern and projected the cells onto two dimensions using uniform manifold approximation and projection (UMAP) (20), and determined cell-type identities of the main clusters using a mouse hippocampal reference panel (21) (Fig. 6A). Each cell cluster contained cells from all six samples without batch effects, and there were no clear clustering differences between the PBS and ASO groups (Fig. 6B). To further confirm cell cluster specificity, we highlighted known marker genes for each cell type and found these key genes to be uniquely expressed in their respective clusters, such as *C1qc* for microglia and *Snap25* for neurons (Fig. 6C to F). By assessing IDOL expression in each cell type, we confirmed that IDOL was highly expressed in microglia and that its expression level was effectively reduced by ASO treatment (data not shown). To determine specific genes and pathways that were altered by IDOL knockdown, we identified differentially expressed genes (DEGs) between PBS- and ASO-treated groups within each cell cluster (Table 1) at  $P < 0.05$  and at a false discovery rate (FDR) of  $< 0.05$ . Microglia and oligodendrocytes had the largest numbers of DEGs between the PBS and ASO groups. Annotation of the DEGs with curated biological pathways revealed the lysosomal pathway as the top enriched biological pathway in microglia. IDOL-ASO treatment upregulated lysosomal/phagocytic genes, such as those for cathepsins (*Ctsb* and *Ctsd*) and CD63, strongly suggesting that knockdown of IDOL enhanced phagocytic function of microglia *in vivo* (Table 1).

To further examine the impact of IDOL ASO treatment on microglia heterogeneity in APP/PS1 mice, we reclustered and projected the microglia cells in two dimensions using t-distributed stochastic neighbor embedding (t-SNE) (22) and identified four distinct subgroups (Fig. 7A) that did not show apparent clustering distinction between PBS and ASO mice (Fig. 7B). The gene expression patterns of subgroups 0 and 1 resembled the signatures of homeostatic microglia, with high expression of marker genes such as *P2ry12* and *Cx3cr1* (Fig. 7C, F, and G), whereas subgroups 2 and 3 resembled disease-associated microglia (DAM), with high expression of marker genes such as *Cst7*, *Trem2*, and *ApoE* (23) (Fig. 7D, F, and G). The separation of subgroups 0 and 3 from subgroups 1 and 2 was mainly due to differential expression of inflammatory genes, such as the cytokine genes *Il1a*, *Il1b*, and *Tnf* (Fig. 7E to G). Interestingly, IDOL-ASO treatment shifted the microglia population to a higher proportion of DAM-like subgroups 2 and 3 (22.45% in PBS group versus 35.36% in ASO group;  $P = 0.04154$  [Fisher exact test]) (Fig. 7A). Consistently, microglia in the ASO group displayed higher expression levels of DAM markers, including *B2m*, *Ctsb*, *Ctsd*, *Lpl*, and *Cd63* (Table 1). It has been shown that DAM cells are abundant near amyloid plaques and actively participate in phagocytic removal of amyloid plaques (23). Thus, this shift in microglial populations in IDOL-ASO-treated mice could plausibly be responsible for the reduced amyloid plaque load.

We also reclustered and projected the general neuronal population onto two dimensions using t-SNE to identify neuronal subtypes (Fig. 8A and B). The CA neurons and the subiculum neurons did not clearly separate, since their gene profiles and physical locations are similar to one another. However, neurons of the dentate gyrus, interneurons, and Cajal-Retzius neurons were clearly separated from the others and demonstrated unique gene expression profiles (Fig. 8C and D). Pathway analysis of the DEGs ( $P < 0.05$ ) revealed that ASO treatment changed the expression of genes enriched

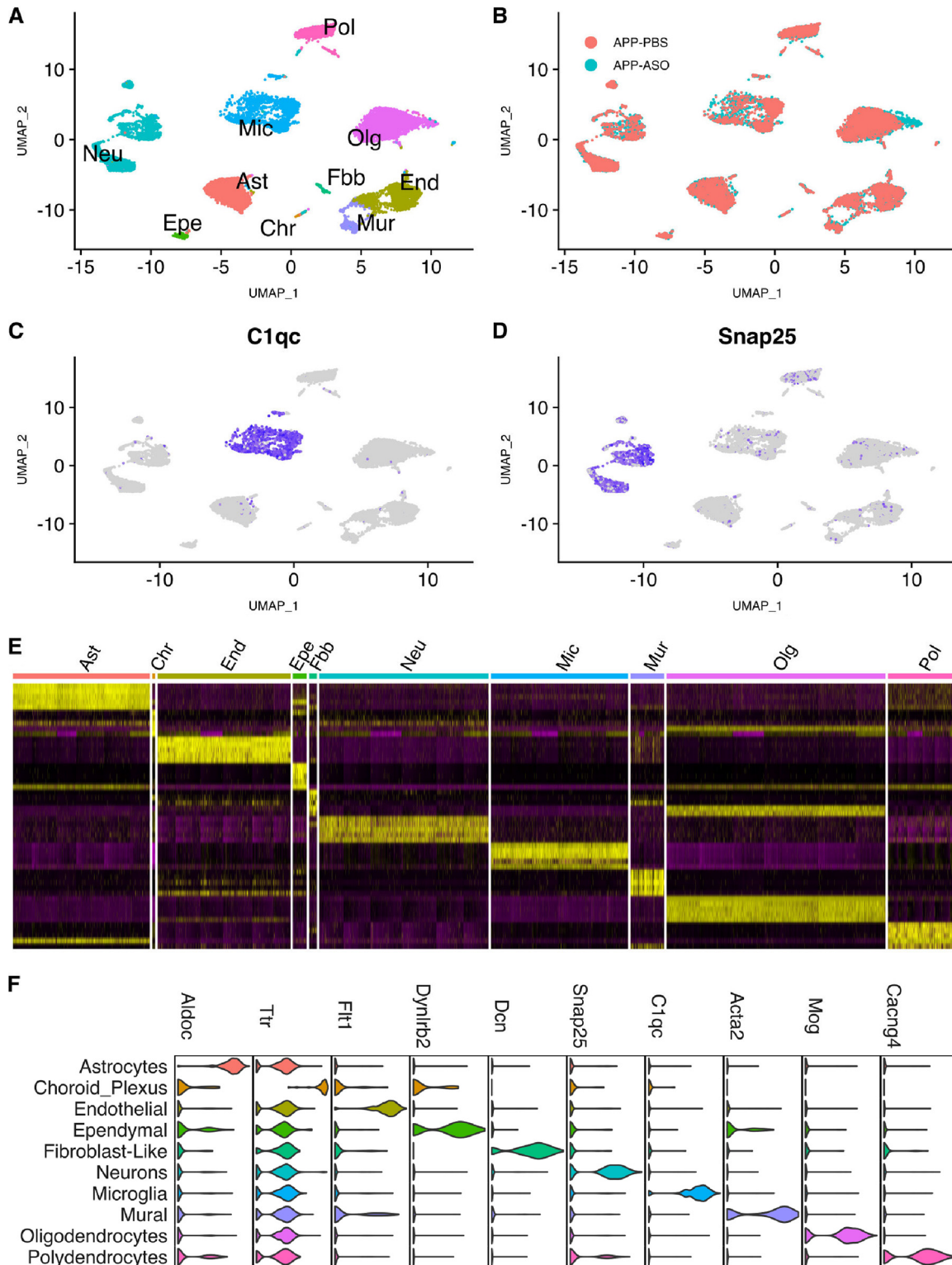


**FIG 6** (A) Uniform manifold approximation and projection (UMAP) dimensionality reduction plot showing hippocampal cell type cluster separation. Each colored dot is a cell and different cell types are labeled with different colors. (B) UMAP plot showing no clear cell type separation by treatment. Red cells originated from PBS-treated mice, and blue cells originated from IDOL ASO-treated mice. (C and D) Feature plot highlighting the expression of known cell markers: *C1qc* for Microglia (C) and *Snap25* for neuron (D). (E) Heat map showing distinct cluster-specific gene expression patterns by plotting the top ten marker genes from each cluster (y axis) against the cell types (x axis). (F) Normalized expression values of top cell-type-specific marker genes are plotted as violin plots, with cell types as rows and genes as columns. Cells were from three PBS- and three ASO-treated mice.

**TABLE 1** Top enriched pathways among DEGs of major cell types (FDR < 5%) and representative DEGs in the select pathways

Cell type	No. of DEGs	Top DEG pathway	Top four or five representative DEGs		
Astrocyte	108 (6)	Cholesterol homeostasis	Up: Clu. Down: Hmgcs1, Cd9, Alcam		
Endothelial	129 (6)	Mtorc1 signaling	Up: Bhlhe40, Hspa9. Down: Gapdh, Hmgcs1, Cd9		
		TNFA signaling via NF-κB	Up: Fosb, Edn1, Egr1. Down: Klf9, Tsc22d1		
		Angiogenesis	Up: Thbd. Down: Vtn, App, Kcnj8		
		P53 pathway	Up: Fos. Down: Fas, Ccnd3, Tsc22d1, App		
		Androgen response	Up: B2m, Elk4. Down: Sepp1, Ccnd3, Tsc22d1		
		UV response up	Up: Fosb, Tfrc, Fos, Ptpd. Down: Ccnd3		
		Amyloids	Up: Ttr, Cst3, B2m. Down: App, H2afz		
		Heme metabolism	Up: Tfrc, Pqlc1. Down: Sec14l1, Slc2a1, Tcea1		
		Focal adhesion	Up: Cav2, Actb. Down: Itga6, Vtn, Ccnd3		
		Fibroblast-like	61	Signaling by insulin receptor	Down: Sos1, Atp6v1e1, Atp6v0b, Eif4g1
mRNA splicing	Down: Hnrnpf, Srsf1, Srsf7, Prpf6				
G <sub>2</sub> /M checkpoint	Down: Srsf1, Ythdc1, Notch2, Amd1				
Processing of capped intron containing pre-mRNA	Down: Hnrnpf, Srsf1, Srsf7, Prpf6				
Hemostasis	Up: Ppp2r5c. Down: App, Zfpm2, Atp1b1, L1cam				
Lysosome	Up: Npc2, Ctsd, Ctsb, Cd63, Hexa				
UV response up	Up: Cxcl2. Down: Ccnd3, Rhob, Lyn, Junb				
GPVI-mediated activation cascade	Down: Rhob, Lyn, Plcg2, Vav1, Pik3r1				
B cell receptor signaling pathway	Down: Lyn, Inpp5d, Plcg2, Jun, Vav1				
Phosphatidylinositol signaling system	Up: Dgkd. Down: Inpp4b, Inpp5d, Plcg2, Pip4k2a				
Microglial macrophage	170 (16)	Androgen response	Up: B2m. Down: Ccnd3, Inpp4b, Fkbp5, Mak		
		Biocarta Ppara pathway	Up: Hsp90aa1, Lpl. Down: Nrip1, Jun, Pik3r1		
		Allograft rejection	Up: B2m, Tlr2. Down: Ccnd3, Ccr5, Lyn		
		Antigen activates B cell receptor leading to generation of second messengers	Down: Lyn, Plcg2, Vav1, Pik3r1		
		Hemostasis	Up: Cd63. Down: Rhob, Slc8a1, Lyn, Dock4		
		Biocarta Fcer1 pathway	Down: Lyn, Jun, Vav1, Pik3r1		
		Fc epsilon Ri signaling pathway	Down: Lyn, Inpp5d, Plcg2, Vav1, Pik3r1		
		Leukocyte transendothelial migration	Up: Cyba. Down: Rhoh, Arhgap5, Plcg2, Vav1		
		TNFA signaling via NF-κB	Up: Tlr2, Cxcl2, Cdkn1a. Down: Rhob, Junb		
		Complement	Up: Ctsd, Ctsb. Down: Lyn, Dock4, Lgmn		
		Inflammatory response	Up: Tlr2, Rgs1, Cdkn1a. Down: Lyn, Stab1		
		Interleukin-2 Stat5 signaling	Up: Cst7, Ctsz. Down: Ccnd3, Rhob, Rhoh		
		Pathways in cancer	Up: Cdkn1a. Down: Tpm3, Tgfb1, Runx1, Plcg2		
		ErbB signaling pathway	Up: Cdkn1a. Down: Plcg2, Jun, Nrg3, Pik3r1		
		Antigen processing and presentation	Up: B2m, Ctsb, Hsp90aa1, Tapbp. Down: Lgmn		
		Apoptosis	Up: Cdkn1a. Down: Rhob, Txnip, Jun, Btg2		
		Signaling by Rho GTPases	Down: Srgap2, Rhob, Rhoh, Ophn1, Arhgap25		
		FcγR-mediated phagocytosis	Down: Lyn, Inpp5d, Plcg2, Vav1, Pik3r1		
		Chemokine signaling pathway	Up: Cxcl2, Ccl3. Down: Elmo1, Ccr5, Lyn		
		Platelet activation signaling and aggregation	Up: Cd63, Dgkd. Down: Rhob, Lyn, Plcg2		
		Toll receptor cascades	Up: Ctsb, Tlr2. Down: Plcg2, Lgmn, Jun		
		Glioma	Up: Cdkn1a, Igf1. Down: Plcg2, Pik3r1		
		<i>Leishmania</i> infection	Up: Tlr2, Cyba. Down: Jun, Ifngr1		
		P53 pathway	Up: Ctsd, Cdkn1a. Down: Ccnd3, Txnip, Jun		
		Chronic myeloid leukemia	Up: Cdkn1a. Down: Tgfb1, Runx1, Pik3r1		
		Mural	88 (1)	Smooth muscle contraction	Up: Lmod1, Calm2, Acta2, Myh11. Down: Tpm4
				Muscle contraction	Up: Lmod1, Calm2, Acta2, Myh11. Down: Tpm4
				Vascular smooth muscle contraction	Up: Rock1, Calm2, Acta2, Myh11. Down: Ramp2
				Myogenesis	Up: Myh11, Smtn. Down: App, Igfbp7, Ablim1
				Integrin cell surface interactions	Down: Pecam1, Lamc1, Bsg, Vtn
Cajal-Retzius neuron	46 (1)	Focal adhesion	Up: Rock1, Mylk. Down: Flt1, Lamc1, Vtn		
		Wnt signaling pathway	Down: Csnk1a1, Tbl1x, Ccnd2, Btrc		
Neuron dentate	90 (2)	Alzheimer's disease	Up: Itpr1. Down: Gapdh, Apbb1, Ndufb4, Ndufc2		
Neuron subiculum	93	Oxidative phosphorylation	Up: Vdac1, Atp5g3, Afg3l2, Cox6b1. Down: Pdhb		
Oligodendrocyte	261 (54)	Cardiac muscle contraction	Up: Cox6a1, Cox7a2, Cacb4, Cox4i1. Down: Atp1b3		
		Pathogenic <i>E. coli</i> infection	Up: Arpc1a, Actb, Arhgef2, Actg1, Ywhaz		
Polydendrocyte	95 (4)	Biocarta Chrebp2 pathway	Up: Ywhaz, Ywhab. Down: Ppp2r2a, Ywhae		
		Cardiac muscle contraction	Up: Cox4i1, Cox6a1. Down: Cacna2d3, Cacna2d1		
		Parkinson's disease	Up: Cox4i1, Cox6a1, Ubb, Atp5e, Pink1		
		Oxidative phosphorylation	Up: Cox4i1, Ldhd, Cox6a1, Atp5e. Down: Timm13		
		Alzheimer's disease	Up: Apoe, Cox4i1, Cox6a1, Atp5e. Down: Gsk3b		
		Amyloids	Up: Ttr, Cst3, Itm2b, B2m		

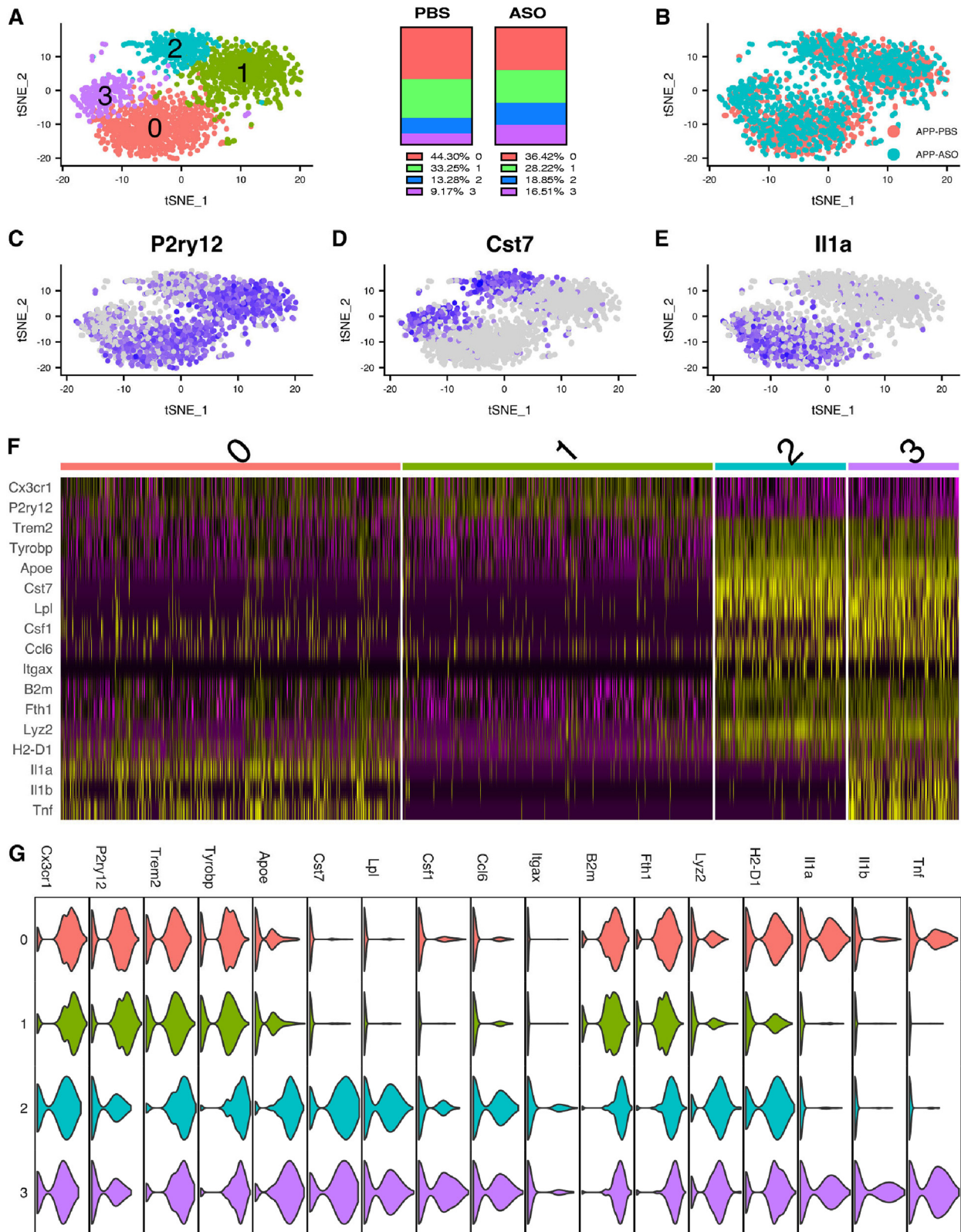


**FIG 7** (A) t-SNE plot showing microglia subtypes. Each colored dot is a cell, microglia subtypes are labeled with different colors (left), and the percentages of each subtypes in each treatment group are indicated (right). (B) t-SNE plot shows no clear separation of microglia subtypes by treatment group. Microglia originating from PBS-treated mice are labeled in red, and microglia originating from IDOL ASO-treated mice are labeled in blue. (C to E) Feature plot highlighting key marker genes for microglia subtypes. *P2ry12*, a homeostatic microglia marker gene; *Cst7*, a disease associated microglia marker gene; *Il1a*, an inflammatory microglia marker gene. (F) Heat map showing the distinct transcriptional patterns of the four microglia subgroups. (G) Normalized expression values of top marker genes for microglia subtypes are plotted as violin plots, with subtypes as rows and genes as columns.

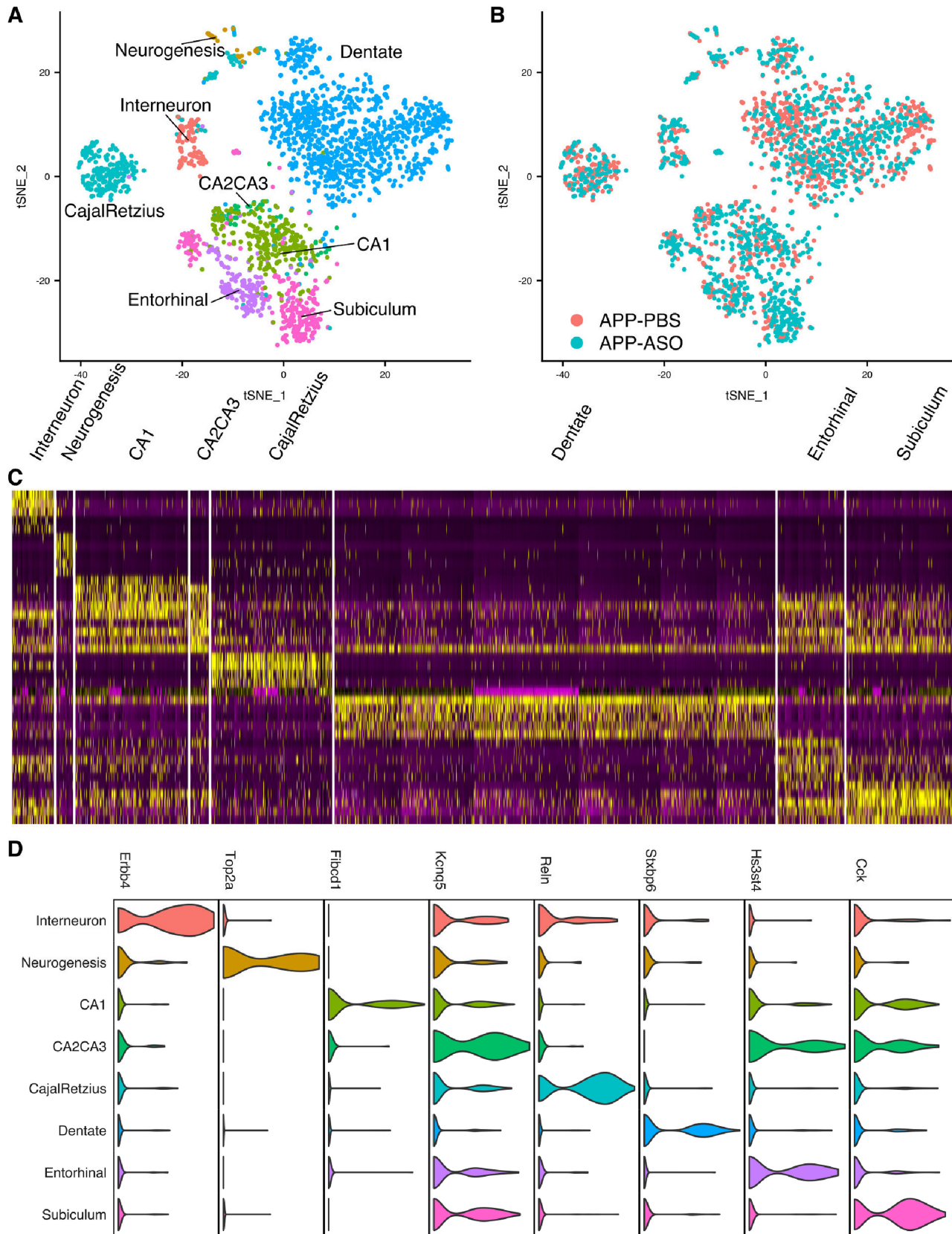


**FIG 8** (A) t-SNE plot showing neuronal subtypes. Each color indicates a different cell type cluster identified. (B) t-SNE plot showing no clear separation of neuronal subtypes by treatment group. Red cells originated from PBS-treated mice, and blue cells originated from IDOL ASO-treated mice. (C) A heat map of Drop-seq defined marker genes of major neuronal subtypes shows distinct gene expression patterns between each neuronal subtype. (D) Normalized expression values of top marker genes for neuronal subtypes are plotted as violin plots, with subtypes as rows and genes as columns.

in the Wnt signaling pathway in Cajal-Retzius neurons, the oxidative phosphorylation pathway in subiculum neurons (mostly pyramidal cells), and the homeostatic responses in interneurons (Table 1).

## DISCUSSION

ApoE4 has a powerful impact on the development of late-onset AD. A $\beta$  turnover and clearance in the mouse brain *in vivo* is strongly dependent upon ApoE isoform (6), suggesting that *APOE* alleles contribute to human AD risk by differentially regulating clearance of A $\beta$  from the brain and that enhancing A $\beta$  clearance may be a therapeutic strategy for AD prevention and treatment. It is reasonable to speculate that the biological effects of ApoE are at least partially mediated by the receptors to which it binds. LDLR is an ApoE receptor known to regulate brain A $\beta$  clearance. LDLR deficiency is associated with increased A $\beta$  deposition in Tg2576 APP-transgenic mice (24, 25), while overexpression of the LDLR in the brain enhances A $\beta$  clearance and decreases A $\beta$  deposition (8). These findings suggest that increasing LDLR levels in brain cells could be beneficial in AD, but it is pivotal to validate tractable approaches to regulate brain LDLR levels in order to translate basic science knowledge to clinical application. We previously identified E3 ubiquitin ligase IDOL as a negative regulator of LDLR proteins levels in microglia and neurons (9). In this study, we examined the effects of IDOL reduction in adult APP/PS1 mice using an anti-IDOL ASO. IDOL inhibition led to a reduction in A $\beta$  pathology, a decrease in neuritic dystrophy around the plaques, and an improvement in spatial memory. This study suggests that pharmacologically inhibiting IDOL could be a feasible approach to ameliorate A $\beta$ -related pathology.

Microglia are professional phagocytes capable of clearing targeted pathogens, cellular debris, and pathogenic A $\beta$  in the brain. Previous *in vitro* studies suggested that loss of IDOL in microglia enhances the uptake and clearance of A $\beta$ . In this study, our scRNA-seq data showed that ASO treatment increased the expression of lysosomal/phagocytic cell-related genes in microglia *in vivo*, corresponding to the enhanced clearance of soluble A $\beta$  and reduced plaque deposition in the brains of APP/PS1 mice. High-level expression of genes in phagocytic and lipid metabolism pathways is the molecular signature of disease-associated microglia (DAM), a recently identified subset of CNS-resident microglia in the 5XFAD mouse model (23). The existence of DAM in mice and humans has recently been confirmed in tauopathy AD models (26, 27), aging (27, 28), and other neurodegenerative diseases, such as amyotrophic lateral sclerosis (ALS) (29) and multiple sclerosis (30). DAM has been shown to associate with amyloid plaques and actively participate in the dismantling and digestion of the amyloid plaques (23). In our exploration of the impact of IDOL on microglia heterogeneity, we found that IDOL-ASO treatment shifted the microglial populations to a higher proportion of DAM-like subgroups (Fig. 6), despite the fact that ASO-treated APP/PS1 mice had lower levels of A $\beta$  and plaque deposition (Fig. 1 and 2). These findings suggest that the IDOL-LDLR pathway regulates the phagocytotic function in microglia in response to A $\beta$  challenge. The underlying mechanisms through which increased LDLR levels enhanced phagocytic function in microglia remain to be clarified.

Since LDLR is a major metabolic receptor for ApoE, the IDOL-LDLR pathway is expected to regulate ApoE uptake and recycling in microglia. It has been reported that ApoE facilitates the microglial response to amyloid plaque pathology (31). We reason that LDLR may enhance phagocytic activity of microglia through the ApoE pathway. Given that ApoE also serves as ligand for TREM2 (32), we further speculate that ApoE may increase phagocytosis of A $\beta$  by enhancing TREM2 signaling. Future experiments will address whether the effect of the IDOL-LDLR pathway on microglial phagocytic function is dependent on ApoE and different ApoE alleles.

When reclustering microglia, we detected two previously identified subtypes: the homeostatic microglia (subgroups 0 and 1) and DAM (subgroups 2 and 3). Within each of these subtypes, we also identified subgroups with different expressions of inflammatory genes, such as *Il1b* and *Tnfa*. Compared to subgroups 1 and 2, microglial subgroups 0 and 3 were enriched for pathways involved in tumor necrosis factor alpha

(TNF- $\alpha$ ) signaling, interferon gamma (IFN- $\gamma$ ) response, and the inflammatory response (FDR <0.05). The exact role of these microglia subgroups in amyloid pathology remains unclear and will be a topic for future investigation. Interestingly, inflammatory cytokine genes (*Il1a*, *Il1b*, and *Tnfa*) were positively associated with the DAM-associated gene *Csf1* in our study (Fig. 6B). CSF-1 is considered a key regulator of inflammatory responses in the brain. Several lines of evidence suggest that microglial activation is mediated by a CSF-1/CSF-1R autocrine loop, which results in reactive microgliosis and the release of inflammatory cytokines (33, 34). Our results are consistent with these previous findings. It has been shown that CSF-1 increases microglial phagocytic activity and stimulates clearance of A $\beta$  (35); however, CSF-1 also mediates microglial-induced neurotoxicity by promoting the release of inflammatory cytokines. Our result showed both homeostatic microglia and DAM can be further divided into subgroups with different *Csf1* expression levels (Fig. 6B). It is plausible that these four subgroups may contribute differently to the pathogenesis of AD. Discovering ways of precisely modulating microglial inflammation and phagocytosis in AD is an exciting area for future investigation.

IDOL is also expressed in neurons, where it posttranslationally regulates the level of neuronal lipoprotein receptors, including ApoER2/LRP8 and VLDLR. IDOL-dependent regulation of synaptic ApoER2 has been implicated in the modulation of dendritic filopodium initiation and synapse maturation during the early postnatal stage (36). ApoER2 has also been shown to functionally couple to NMDA receptors (37) and to protect against the loss of cortical neurons during normal aging (38). IDOL ASO treatment increased brain ApoER2 levels in our study (Fig. 1C). Our scRNAseq results yielded only small number of DEGs in neurons between PBS and ASO groups when comparing to microglia, suggesting that knockdown of IDOL has more a prominent impact on microglial functions. However, we cannot rule out the possibility that enhanced neuronal ApoER2 levels also contribute to the neuroprotective effects of IDOL knockdown, such as the decreased neuritic dystrophy around the plaques. We are in the process of evaluating the impact of neuron- and microglia-specific IDOL deletion on neuropathological progression and cognitive function in AD mouse models. The results from these studies will offer a better understanding of the mechanisms through which IDOL impacts AD-related pathology.

## MATERIALS AND METHODS

**Animals.** Male C57BL/6J (000664) and B6.Cg-Tg(APP<sup>swe</sup>,PSEN1<sup>dE9</sup>)85Dbo/Mmjax (005864) mice were purchased from The Jackson Laboratory. All mouse experiments were approved and performed under the guidelines of the Animal Care and Research Advisory Committees at the University of California, Los Angeles (UCLA).

**Antibodies and reagents.** Primary antibodies used in this study are: anti-human amyloid  $\beta$  (N) (82E1) from IBL Co., Ltd.; anti-amyloid precursor protein antibody [Y188] (ab32136), anti-apolipoprotein E antibody (ab183596), anti-ApoER2 antibody (ab108208), and anti-LAMP1 antibody (ab25245) from Abcam; anti-LDL receptor polyclonal antibody from Cayman; anti-Iba1 antibody from Wako; and anti-gial fibrillary acidic protein (anti-GFAP) from Dako. Anti-VLDLR antibody was a gift from Joachim Herz, University of Texas Southwestern Medical Center. All secondary antibodies were purchased from Thermo Fisher or Jackson ImmunoResearch. Antisense oligonucleotides (ASOs) targeting IDOL (5'-TTCCCTTTTTC CACACGCCA-3') were provided by Ionis Pharmaceuticals, Carlsbad CA. Complete ASO chemistry information was as follows. IDOL ASO (Tes Tes mCes mCeo Tes Tds Tds Tds Tds Tds mCds mCds Ads mCds Ads mCeo Ges mCes mCes Ae), where capital letters indicate base abbreviation, m is 5-methylcytosine, e is 2'-O-methoxyethylribose (MOE), k is (S)-2',4'-onstrained 2'-O-ethyl (cEt), d is deoxyribose, s is phosphorothioate, and o is phosphodiester. When administering IDOL ASO to a cohort of wild-type mice (two groups,  $n = 5$  for each group), IDOL mRNA levels were downregulated 92 and 62%, respectively, 1 week or 2 months after ASO administration. The half-life of ASO was estimated around 9 weeks.

**mRNA analysis.** mRNA level was determined by real-time RT-qPCR (Diagenode, Denville, NJ) from RNA isolated from frozen tissues with TRIzol (Life Technologies, Carlsbad, CA) according the manufacturer's instructions. Statistical analysis was conducted using a two-tailed unpaired  $t$  test or one-way ANOVA.

**Protein analysis.** Proteins were sequentially extracted from brain tissues with RIPA, and 5 M guanidine buffer in the presence of protease inhibitors as described previously (9). For Western blots, equal amounts of proteins (10 to 40 mg) were separated on NuPAGE bis-tris gels (Invitrogen), and membranes were probed with primary and secondary antibodies. Signals were visualized by chemiluminescence (ECL Plus; GE Healthcare). Blots were quantified by densitometry with ImageJ software (National Institutes of Health [NIH]). To quantify A $\beta$ 40 (KHB3481) and A $\beta$ 42 (KHB3441), human ELISA kits

from Life Technologies were used. Statistical analysis was conducted using a two-tailed unpaired *t* test or one-way analysis of variance (ANOVA).

**Histological analysis.** Brains were sectioned on a cryostat at a 40- $\mu$ m thickness. For immunofluorescence staining, free-floating sections were blocked with PBS containing 10% normal goat serum (NGS) at room temperature for 30 min, incubated with primary antibody in blocking solution at 4°C overnight, and then incubated with secondary antibody at room temperature for 1 h. Sections were mounted on slides with ProLong Diamond (Life Technologies). For immunohistochemistry, free-floating sections were treated with 0.3% H<sub>2</sub>O<sub>2</sub> and blocked with 3% NGS. Sections were then incubated with biotinylated 82E1 (1:500) or anti-Iba1 (1:1,000) in blocking solution at 4°C for 24 h. Sections were incubated with biotinylated anti-rat or anti-rabbit IgG antibody (Vector Laboratories) in blocking solution at room temperature for 1 h. Antibody binding was detected with Vectastain ABC Elite (Vector Laboratories) and DAB peroxidase (horseradish peroxidase) substrate kits (Vector Laboratories) supplemented with nickel solution. Sections were dehydrated and mounted on slides with Permount (Fisher Scientific). Images were captured on a confocal microscopy (Zeiss) and quantified using ImageJ software. Statistical analysis was conducted using a two-tailed unpaired *t* test or one-way ANOVA.

**Behavior tests. (i) Morris water maze test.** The Morris water maze is a stainless-steel circular tank with a 200-cm diameter. The tank is filled with water dyed with white, using liquid tempera paint to make the water opaque. A platform is placed in one of the quadrants of the pool and submerged 1 cm below the surface. During the trial, mice were placed in the desired start position facing the tank wall and released into the water at water level. If a mouse failed to find the platform within 60 s, it was then placed on the platform for 15 s before being removed. Mice were then placed at a new start location, and the trial repeated four times/day. On day 6, the probe test (wherein the mouse was allowed to free swim for 60 s with the submerged platform removed) was conducted. The percent time spent in the goal quadrant was calculated and analyzed for each mouse. The experimenter was blind to the genotype of the animals. Behavioral data from the training period were analyzed using repeated-measures ANOVA. Data from the probe test were analyzed using one-way ANOVA. Data from the visual cue test were analyzed using a two-tailed unpaired *t* test or repeated-measures ANOVA. All behavioral data were analyzed in Prism 7 (GraphPad Software, Inc.).

**(ii) Fear conditioning.** To assess fear conditioning, mice were placed in a shock chamber (Med Associates, Inc.) on day 1 for a 7-min training period; during the last 5 min, the mice were exposed to three pairings (1-min intervals) of a 20-s tone immediately followed by a 2-s, 0.38-mA foot shock. On day 2, the mice were placed in the training context for 5 min, and the level of freezing was recorded. On day 3, the mice were placed in a different context for 6 min, and during the last 3 min the tone was played. Mouse freezing was recorded with the FreezeFrame program and analyzed using the FreezeView program.

Normal nociception of all animal strains was ascertained by registering. One-way ANOVA was used to analyze the percent freezing scores of the contextual and cue-dependent freezing. All behavioral data were analyzed in Prism 7.

**(iii) Single cell preparation.** Single-cell suspensions from bulk tissue were generated as previously described (39) at a final concentration of 100 cells/ $\mu$ l in 0.01% bovine serum albumin (BSA)-PBS by digesting freshly dissected hippocampus tissue with papain (Worthington, Lakewood, NJ). Briefly, the hippocampus was rapidly dissected and transferred into 4 ml of ice-cold Hibernate A (HA; BrainBits LLC, Springfield, IL)-B27 (Invitrogen, Carlsbad, CA)-GlutaMAX (Fisher Scientific, Hampton, NH) (HABG) and then incubated in a water bath at 30°C for 8 min (40). The supernatant was discarded, and the remaining tissue was incubated with papain (12 mg in 6 ml of HA-Ca) at 30°C for 30 min. After incubation, the papain solution was removed from the tissue and washed with HABG three times. Using a siliconized 9-in Pasteur pipette with a fire-polished tip, the suspension was triturated approximately ten times in 45 s. Next, the cell suspension was carefully applied to the top of the prepared Opti-Prep density gradient (Sigma-Aldrich, St. Louis, MO). The gradient was then centrifuged at 800  $\times g$  for 15 min at 22°C. We aspirated the top 6 ml containing cellular debris. To dilute the gradient material, we mixed the desired cell fractions with 5 ml of HABG. The cell suspension containing the desired cell fractions was centrifuged for 3 min at 22°C at 200  $\times g$ , and the supernatant containing the debris was discarded. Finally, the cell pellet was loosened by flicking the tube, and the cells were resuspended in 1 ml of 0.01% BSA (in PBS). This final cell suspension solution was passed through a 40- $\mu$ m strainer (Fisher Scientific) to discard debris, followed by cell counting.

**(iv) Drop-seq single-cell barcoding, library preparation, and sequencing.** Drop-seq was performed as previously described (19), with the following modifications: (i) the number of beads in a single PCR tube was increased to 4,000/tube, (ii) the number of PCR cycles was increased to 4 + 11 cycles, and (iii) multiple PCR tubes were pooled prior to size selection and purification with AMPure XP (Beckman Coulter, Brea, CA). The amplified cDNAs were then checked using the Agilent TapeStation system (Agilent, Santa Clara, CA) for library quality, average size, and concentration estimation. The samples were then tagmented using a Nextera DNA library preparation kit (Illumina, San Diego, CA), and multiplex indices were added. The Drop-seq library molar concentration was determined by Qubit fluorometric quantitation (Thermo Fisher, Canoga Park, CA), and library fragment length was estimated using a TapeStation. Sequencing was performed on an Illumina HiSeq 4000 (Illumina, San Diego, CA) instrument using the Drop-seq custom read 1B primer (IDT, Coralville, IA). 100-bp paired-end reads were generated with an 8-bp index read for multiplexing. Read 1 consists of the 12-bp cell barcode, followed by the 8-bp unique molecular identifier (UMI). Read 2 contains the single cell transcripts.

**(v) Drop-seq data preprocessing and quality control.** The demultiplexed fastq files from the Drop-seq sequencing data were processed into a digital gene expression matrix using the dropSeqPipe

(<https://github.com/Hoohm/dropSeqPipe>) SnakeMake wrapper for Drop-seq tools version 1.13. Briefly, read pairs with quality score of  $<10$  were discarded, transcript reads were trimmed to remove TSO contamination, and poly(A) tails and then aligned to mm10 using STAR v2.5.0c with default settings. A digital gene expression matrix for each sample was generated, wherein each row is the read count of a gene, and each column represents a unique cell. The transcript counts of each cell were normalized by the total number of UMIs for that cell. These values were then multiplied by 10,000 and Ln transformed. Digital gene expression matrices from the six samples (three PBS- and three ASO-treated samples) were combined to create a pooled digital gene expression matrix. Single cells were identified from background noise by using a threshold of at least 250 genes and 500 transcripts.

**(vi) Identification of cell clusters.** The Seurat R package (version 2.3.1; <https://github.com/satijalab/seurat>) was used to project all sequenced cells onto two dimensions using uniform manifold approximation and projection (UMAP), and Louvain modularity clustering (41) was used to define clusters. To further refine the microglia and neuronal cell clusters, clusters expressing either microglia- or neuron-specific markers were pooled, projected onto two dimensions using t-distributed stochastic neighbor embedding (t-SNE), and reanalyzed separately in a similar fashion, only considering this microglia or neuronal subset. Briefly, the most highly variable genes were identified using the mean and dispersion (variance/mean), which were used to scale and center the data. Principal component analysis was performed on this normalized data, and significant principal components were identified using the JackStraw permutation-based approach (42). These significant PCs were used in t-SNE and UMAP to project the data onto two dimensions, and graph-based clustering was used to identify cell clusters.

**(vii) Resolving cell identities of the cell clusters.** To resolve the identities of the cell clusters, the single-cell data were mapped with a hippocampal reference data set (21) using FindTransferAnchors and TransferData in the Seurat Package (43). Cell types were confirmed by comparing marker genes to known markers for hippocampal cell types and neuronal subtypes (44–46). These markers were sufficient to confirm all major cell types, as well as neuronal subpopulations.

**(viii) Identification of differentially expressed genes (DEGs).** Differentially expressed genes were determined using FindAllMarkers in the Seurat Package. The log fold change was 0.25, and the minimum fraction of cells expressing each gene was set at 0.10. The Wilcoxon test was used to determine differential expression. The Benjamini-Hochberg procedure was used to correct multiple testing, and an FDR threshold of 0.05 was used to determine differentially expressed genes.

**(ix) Pathway analysis of DEGs.** *P* values for enriched pathways were determined using a hypergeometric distribution, taking into account the number of overlapping differentially expressed genes with a pathway, the total number of genes in the pathway, and the total number of genes, and the total number of differentially expressed genes. All pathways were determined significant or suggestive with a Bonferroni corrected *P* value of 0.05. Significant pathways were determined with Benjamini-Hochberg corrected differentially expressed genes at a threshold of 0.05. Suggestive pathways were determined with differentially expressed genes at a *P* value threshold of 0.01.

**Data availability.** The sequencing data have been deposited to GEO under accession number [GSE142535](https://www.ncbi.nlm.nih.gov/geo/query/acc.cgi?acc=GSE142535).

## ACKNOWLEDGMENTS

We thank Joachim Herz for sharing antibodies to ApoER2 and VLDLR; Jon Salazar for genotyping and mouse care; Marcus Tol, Stephen D Lee, and Jaspreet Sandhu for technical support and extensive discussions on the project; and Ingrid Cely for technical support on the single cell experiments.

This research was supported by NIH grants R00 AG054736 (to J.G.). R.L. is supported by NIH-NCI National Cancer Institute grant T32CA201160. X.Y. is supported by NIH grants R01 DK104363 and R21 NS103088.

We declare there are no competing financial interests.

Author contributions were as follows: Jie Gao, conceptualization, formal analysis, supervision, funding acquisition, investigation, writing of the original draft, project administration, and review and editing of the manuscript; Russell Littman, single cell data analysis and review and editing of the manuscript; In Sook Ahn and Graciél Diamante, single-cell RNA sequencing experiments and review and editing of the manuscript; Xu Xiao helped with behavior testing; Xia Yang, analysis, supervision, and review and editing of the manuscript; and Peter Tontonoz, formal analysis, supervision, and review and editing of the manuscript.

## REFERENCES

1. Corder EH, Saunders AM, Strittmatter WJ, Schmechel DE, Gaskell PC, Small GW, Roses AD, Haines JL, Pericak-Vance MA. 1993. Gene dose of apolipoprotein E type 4 allele and the risk of Alzheimer's disease in late onset families. *Science* 261:921–923. <https://doi.org/10.1126/science.8346443>.
2. Liu CC, Kanekiyo T, Xu H, Bu G. 2013. Apolipoprotein E and Alzheimer disease: risk, mechanisms, and therapy. *Nat Rev Neurol* 9:106–118. <https://doi.org/10.1038/nrneuro.2012.263>.
3. Shi Y, Alzheimer's Disease Neuroimaging Initiative, Yamada K, Liddelov SA, Smith ST, Zhao L, Luo W, Tsai RM, Spina S, Grinberg LT, Rojas JC, Gallardo G, Wang K, Roh J, Robinson G, Finn MB, Jiang H, Sullivan PM,

- Baufeld C, Wood MW, Sutphen C, McCue L, Xiong C, Del-Aguila JL, Morris JC, Cruchaga C, Alzheimer's DNI, Fagan AM, Miller BL, Boxer AL, Seeley WW, Butovsky O, Barres BA, Paul SM, Holtzman DM. 2017. ApoE4 markedly exacerbates tau-mediated neurodegeneration in a mouse model of tauopathy. *Nature* 549:523–527. <https://doi.org/10.1038/nature24016>.
4. Huynh TV, Liao F, Francis CM, Robinson GO, Serrano JR, Jiang H, Roh J, Finn MB, Sullivan PM, Esparza TJ, Stewart FR, Mahan TE, Ulrich JD, Cole T, Holtzman DM. 2017. Age-dependent effects of apoE reduction using antisense oligonucleotides in a model of beta-amyloidosis. *Neuron* 96:1013–1023. <https://doi.org/10.1016/j.neuron.2017.11.014>.
  5. Ma J, Yee A, Brewer HB, Das S, Potter H. 1994. Amyloid-associated proteins alpha 1-antichymotrypsin and apolipoprotein E promote assembly of Alzheimer beta-protein into filaments. *Nature* 372:92–94. <https://doi.org/10.1038/372092a0>.
  6. Castellano JM, Kim J, Stewart FR, Jiang H, DeMattos RB, Patterson BW, Fagan AM, Morris JC, Mawuenyega KG, Cruchaga C, Goate AM, Bales KR, Paul SM, Bateman RJ, Holtzman DM. 2011. Human apoE isoforms differentially regulate brain amyloid- $\beta$  peptide clearance. *Sci Transl Med* 3:89ra57. <https://doi.org/10.1126/scitranslmed.3002156>.
  7. Holtzman DM, Herz J, Bu G. 2012. Apolipoprotein E and apolipoprotein E receptors: normal biology and roles in Alzheimer disease. *Cold Spring Harb Perspect Med* 2:a006312. <https://doi.org/10.1101/cshperspect.a006312>.
  8. Kim J, Castellano JM, Jiang H, Basak JM, Parsadanian M, Pham V, Mason SM, Paul SM, Holtzman DM. 2009. Overexpression of low-density lipoprotein receptor in the brain markedly inhibits amyloid deposition and increases extracellular A beta clearance. *Neuron* 64:632–644. <https://doi.org/10.1016/j.neuron.2009.11.013>.
  9. Choi J, Gao J, Kim J, Hong C, Kim J, Tontonoz P. 2015. The E3 ubiquitin ligase Idol controls brain LDL receptor expression, ApoE clearance, and A $\beta$  amyloidosis. *Sci Transl Med* 7:314ra184. <https://doi.org/10.1126/scitranslmed.aad1904>.
  10. Gowrishankar S, Yuan P, Wu Y, Schrag M, Paradise S, Grutzendler J, De Camilli P, Ferguson SM. 2015. Massive accumulation of luminal protease-deficient axonal lysosomes at Alzheimer's disease amyloid plaques. *Proc Natl Acad Sci U S A* 112:E3699–E3708. <https://doi.org/10.1073/pnas.1510329112>.
  11. Cras P, Kawai M, Lowery D, Gonzalez-DeWhitt P, Greenberg B, Perry G. 1991. Senile plaque neurites in Alzheimer disease accumulate amyloid precursor protein. *Proc Natl Acad Sci U S A* 88:7552–7556. <https://doi.org/10.1073/pnas.88.17.7552>.
  12. Vorhees CV, Williams MT. 2006. Morris water maze: procedures for assessing spatial and related forms of learning and memory. *Nat Protoc* 1:848–858. <https://doi.org/10.1038/nprot.2006.116>.
  13. Curzon P, Rustay NR, Browman KE. 2009. Cued and contextual fear conditioning for rodents, chapter 2. In Buccafusco JJ (ed), *Methods of behavior analysis in neuroscience*. CRC Press/Taylor & Francis, Boca Raton, FL.
  14. Gosselin D, Link VM, Romanoski CE, Fonseca GJ, Eichenfield DZ, Spann NJ, Stender JD, Chun HB, Garner H, Geissmann F, Glass CK. 2014. Environment drives selection and function of enhancers controlling tissue-specific macrophage identities. *Cell* 159:1327–1340. <https://doi.org/10.1016/j.cell.2014.11.023>.
  15. Gosselin D, Skola D, Coufal NG, Holtman IR, Schlachetzki JCM, Sajti E, Jaeger BN, O'Connor C, Fitzpatrick C, Pasillas MP, Pena M, Adair A, Gonda DD, Levy ML, Ransohoff RM, Gage FH, Glass CK. 2017. An environment-dependent transcriptional network specifies human microglia identity. *Science* 356:eaal3222. <https://doi.org/10.1126/science.aal3222>.
  16. Li Q, Cheng Z, Zhou L, Darmanis S, Neff NF, Okamoto J, Gulati G, Bennett ML, Sun LO, Clarke LE, Marschallinger J, Yu G, Quake SR, Wyss-Coray T, Barres BA. 2019. Developmental heterogeneity of microglia and brain myeloid cells revealed by deep single-cell RNA sequencing. *Neuron* 101:207–223. <https://doi.org/10.1016/j.neuron.2018.12.006>.
  17. Böttcher C, Schlickeiser S, Sneeboer MAM, Kunkel D, Knop A, Paza E, Fidzinski P, Kraus L, Snijders GJL, Kahn RS, Schulz AR, Mei HE, NBB-Psy, Hol EM, Siegmund B, Glauben R, Spruth EJ, de Witte LD, Priller J. 2019. Human microglia regional heterogeneity and phenotypes determined by multiplexed single-cell mass cytometry. *Nat Neurosci* 22:78–90. <https://doi.org/10.1038/s41593-018-0290-2>.
  18. Hammond TR, Dufort C, Dissing-Olesen L, Giera S, Young A, Wysoker A, Walker AJ, Gergits F, Segel M, Nemes J, Marsh SE, Saunders A, Macosko E, Ginhoux F, Chen J, Franklin RJM, Piao X, McCarroll SA, Stevens B. 2018. Single-cell RNA sequencing of microglia throughout the mouse lifespan and in the injured brain reveals complex cell-state changes. *Immunity* 50:253–271. <https://doi.org/10.1016/j.immuni.2018.11.004>.
  19. Macosko EZ, Basu A, Satija R, Nemes J, Shekhar K, Goldman M, Tirosh I, Bialas AR, Kamitaki N, Martersteck EM, Trombetta JJ, Weitz DA, Sanes JR, Shalek AK, Regev A, McCarroll SA. 2015. Highly parallel genome-wide expression profiling of individual cells using nanoliter droplets. *Cell* 161:1202–1214. <https://doi.org/10.1016/j.cell.2015.05.002>.
  20. McInnes L, Healy J, Melville J. 2018. Umap: uniform manifold approximation and projection for dimension reduction. arXiv 1802.03426.
  21. Saunders A, Macosko EZ, Wysoker A, Goldman M, Krienen FM, de Rivera H, Bien E, Baum M, Bortolin L, Wang S, Goeva A, Nemes J, Kamitaki N, Brumbaugh S, Kulp D, McCarroll SA. 2018. Molecular diversity and specializations among the cells of the adult mouse brain. *Cell* 174:1015–1030.e16. <https://doi.org/10.1016/j.cell.2018.07.028>.
  22. Maaten LVD, Hinton G. 2008. Visualizing data using t-SNE. *J Machine Learning Res* 9:2579–2605.
  23. Keren-Shaul H, Spinrad A, Weiner A, Matcovitch-Natan O, Dvir-Szternfeld R, Ulland TK, David E, Baruch K, Lara-Astaiso D, Toth B, Itzkovitz S, Colonna M, Schwartz M, Amit I. 2017. A unique microglia type associated with restricting development of Alzheimer's disease. *Cell* 169:1276–1290. <https://doi.org/10.1016/j.cell.2017.05.018>.
  24. Cao D, Fukuchi K, Wan H, Kim H, Li L. 2006. Lack of LDL receptor aggravates learning deficits and amyloid deposits in Alzheimer transgenic mice. *Neurobiol Aging* 27:1632–1643. <https://doi.org/10.1016/j.neurobiolaging.2005.09.011>.
  25. Katsouri L, Georgopoulos S. 2011. Lack of LDL receptor enhances amyloid deposition and decreases glial response in an Alzheimer's disease mouse model. *PLoS One* 6:e21880. <https://doi.org/10.1371/journal.pone.0021880>.
  26. Friedman BA, Srinivasan K, Ayalon G, Meilandt WJ, Lin H, Huntley MA, Cao Y, Lee SH, Haddick PCG, Ngu H, Modrusan Z, Larson JL, Kaminker JS, van der Brug MP, Hansen DV. 2018. Diverse brain myeloid expression profiles reveal distinct microglial activation states and aspects of Alzheimer's disease not evident in mouse models. *Cell Rep* 22:832–847. <https://doi.org/10.1016/j.celrep.2017.12.066>.
  27. Mrdjen D, Pavlovic A, Hartmann FJ, Schreiner B, Utz SG, Leung BP, Lelios I, Heppner FL, Kipnis J, Merkler D, Greter M, Becher B. 2018. High-dimensional single-cell mapping of central nervous system immune cells reveals distinct myeloid subsets in health, aging, and disease. *Immunity* 48:380–395. <https://doi.org/10.1016/j.immuni.2018.01.011>.
  28. Olah M, Patrick E, Villani AC, Xu J, White CC, Ryan KJ, Piehowski P, Kapasi A, Nejad P, Cimpean M, Connor S, Yung CJ, Frangieh M, McHenry A, Elyaman W, Petyuk V, Schneider JA, Bennett DA, De Jager PL, Bradshaw EM. 2018. A transcriptomic atlas of aged human microglia. *Nat Commun* 9:539. <https://doi.org/10.1038/s41467-018-02926-5>.
  29. Spiller KJ, Restrepo CR, Khan T, Dominique MA, Fang TC, Canter RG, Roberts CJ, Miller KR, Ransohoff RM, Trojanowski JQ, Lee VM. 2018. Microglia-mediated recovery from ALS-relevant motor neuron degeneration in a mouse model of TDP-43 proteinopathy. *Nat Neurosci* 21:329–340. <https://doi.org/10.1038/s41593-018-0083-7>.
  30. Krasemann S, Madore C, Cialic R, Baufeld C, Calcagno N, El Fatimy R, Beckers L, O'Loughlin E, Xu Y, Fanek Z, Greco DJ, Smith ST, Sweet G, Humulock Z, Zrzavy T, Conde-Sanroman P, Gacias M, Weng Z, Chen H, Tjon E, Mazaheri F, Hartmann K, Madi A, Ulrich JD, Glatzel M, Worthmann A, Heeren J, Budnik B, Lemere C, Ikezu T, Heppner FL, Litvak V, Holtzman DM, Lassmann H, Weiner HL, Ochando J, Haass C, Butovsky O. 2017. The TREM2-APOE pathway drives the transcriptional phenotype of dysfunctional microglia in neurodegenerative diseases. *Immunity* 47:566–581.e9. <https://doi.org/10.1016/j.immuni.2017.08.008>.
  31. Colonna M, Butovsky O. 2017. Microglia function in the central nervous system during health and neurodegeneration. *Annu Rev Immunol* 35:441–468. <https://doi.org/10.1146/annurev-immunol-051116-052358>.
  32. Yeh FL, Wang Y, Tom I, Gonzalez LC, Sheng M. 2016. TREM2 binds to apolipoproteins, including APOE and CLU/APOJ, and thereby facilitates uptake of amyloid-beta by microglia. *Neuron* 91:328–340. <https://doi.org/10.1016/j.neuron.2016.06.015>.
  33. Chitu V, Stanley ER. 2006. Colony-stimulating factor-1 in immunity and inflammation. *Curr Opin Immunol* 18:39–48. <https://doi.org/10.1016/j.coi.2005.11.006>.
  34. Hao AJ, Dheen ST, Ling EA. 2002. Expression of macrophage colony-stimulating factor and its receptor in microglia activation is linked to teratogen-induced neuronal damage. *Neuroscience* 112:889–900. [https://doi.org/10.1016/S0306-4522\(02\)00144-6](https://doi.org/10.1016/S0306-4522(02)00144-6).
  35. Mitrasinovic OM, Vincent VA, Simsek D, Murphy GM. 2003. Macrophage colony stimulating factor promotes phagocytosis by murine microglia.

- Neurosci Lett 344:185–188. [https://doi.org/10.1016/S0304-3940\(03\)00474-9](https://doi.org/10.1016/S0304-3940(03)00474-9).
36. Gao J, Marosi M, Choi J, Achiro JM, Kim S, Li S, Otis K, Martin KC, Portera-Cailliau C, Tontonoz P. 2017. The E3 ubiquitin ligase IDOL regulates synaptic ApoER2 levels and is important for plasticity and learning. *Elife* 6:e29178. <https://doi.org/10.7554/eLife.29178>.
  37. Beffert U, Weeber EJ, Durudas A, Qiu S, Masiulis I, Sweatt JD, Li WP, Adelman G, Frotscher M, Hammer RE, Herz J. 2005. Modulation of synaptic plasticity and memory by Reelin involves differential splicing of the lipoprotein receptor Apoer2. *Neuron* 47–579. <https://doi.org/10.1016/j.neuron.2005.07.007>.
  38. Beffert U, Nematollah Farsian F, Masiulis I, Hammer RE, Yoon SO, Giehl KM, Herz J. 2006. ApoE receptor 2 controls neuronal survival in the adult brain. *Curr Biol* 16:2446–2452. <https://doi.org/10.1016/j.cub.2006.10.029>.
  39. Arneson D, Zhang G, Ying Z, Zhuang Y, Byun HR, Ahn IS, Gomez-Pinilla F, Yang X. 2018. Single cell molecular alterations reveal target cells and pathways of concussive brain injury. *Nat Commun* 9:3894. <https://doi.org/10.1038/s41467-018-06222-0>.
  40. Poon K, Barson JR, Fagan SE, Leibowitz SF. 2012. Developmental changes in embryonic hypothalamic neurons during prenatal fat exposure. *Am J Physiol Endocrinol Metab* 303:E432–E441. <https://doi.org/10.1152/ajpendo.00238.2012>.
  41. Blondel VD, Guillaume J-L, Lambiotte R, Lefebvre E. 2008. Fast unfolding of communities in large networks. *J Stat Mech* 2008:P10008. <https://doi.org/10.1088/1742-5468/2008/10/P10008>.
  42. Chung NC, Storey JD. 2015. Statistical significance of variables driving systematic variation in high-dimensional data. *Bioinformatics* 31:545–554. <https://doi.org/10.1093/bioinformatics/btu674>.
  43. Stuart T, Butler A, Hoffman P, Hafemeister C, Papalexi E, Mauck WM, Hao Y, Stoeckius M, Smibert P, Satija R. 2019. Comprehensive integration of single-cell data. *Cell* 177:1888–1902. <https://doi.org/10.1016/j.cell.2019.05.031>.
  44. Romanov RA, Zeisel A, Bakker J, Girach F, Hellysaz A, Tomer R, Alpár A, Mulder J, Clotman F, Keimpema E, Hsueh B, Crow AK, Martens H, Schwindling C, Calvigioni D, Bains JS, Máté Z, Szabó G, Yanagawa Y, Zhang M-D, Rendeiro A, Farlik M, Uhlén M, Wulff P, Bock C, Broberger C, Deisseroth K, Hökfelt T, Linnarsson S, Horvath TL, Harkany T. 2017. Molecular interrogation of hypothalamic organization reveals distinct dopamine neuronal subtypes. *Nat Neurosci* 20:176–188. <https://doi.org/10.1038/nn.4462>.
  45. Chen R, Wu X, Jiang L, Zhang Y. 2017. Single-cell RNA-seq reveals hypothalamic cell diversity. *Cell Rep* 18:3227–3241. <https://doi.org/10.1016/j.celrep.2017.03.004>.
  46. Campbell JN, Macosko EZ, Fenselau H, Pers TH, Lyubetskaya A, Tenen D, Goldman M, Versteegen AM, Resch JM, McCarroll SA, Rosen ED, Lowell BB, Tsai LT. 2017. A molecular census of arcuate hypothalamus and median eminence cell types. *Nat Neurosci* 20:484–496. <https://doi.org/10.1038/nn.4495>.